

Asymmetric scattering of flexural waves in a parity-time symmetric metamaterial beam

Qian Wu, Yangyang Chen, and Guoliang Huang

Citation: *The Journal of the Acoustical Society of America* **146**, 850 (2019); doi: 10.1121/1.5116561

View online: <https://doi.org/10.1121/1.5116561>

View Table of Contents: <https://asa.scitation.org/toc/jas/146/1>

Published by the *Acoustical Society of America*

ARTICLES YOU MAY BE INTERESTED IN

[Non-reciprocal wave phenomena in energy self-reliant gyric metamaterials](#)

The Journal of the Acoustical Society of America **146**, 789 (2019); <https://doi.org/10.1121/1.5114916>

[Introduction to the special issue on non-reciprocal and topological wave phenomena in acoustics](#)

The Journal of the Acoustical Society of America **146**, 719 (2019); <https://doi.org/10.1121/1.5119133>

[Asymmetric acoustic energy transport in non-Hermitian metamaterials](#)

The Journal of the Acoustical Society of America **146**, 863 (2019); <https://doi.org/10.1121/1.5114919>

[Non-reciprocal wave propagation in mechanically-modulated continuous elastic metamaterials](#)

The Journal of the Acoustical Society of America **146**, 782 (2019); <https://doi.org/10.1121/1.5115019>

[A comparison study between acoustic topological states based on valley Hall and quantum spin Hall effects](#)

The Journal of the Acoustical Society of America **146**, 721 (2019); <https://doi.org/10.1121/1.5115017>

[Nonreciprocal acoustic propagation and leaky-wave radiation in a waveguide with flow](#)

The Journal of the Acoustical Society of America **146**, 802 (2019); <https://doi.org/10.1121/1.5115018>



WHY PUBLISH WITH US?

Asymmetric scattering of flexural waves in a parity-time symmetric metamaterial beam

Qian Wu, Yangyang Chen, and Guoliang Huang^{a)}

Department of Mechanical and Aerospace Engineering, University of Missouri, Columbia, Missouri 65211, USA

(Received 25 January 2019; revised 14 May 2019; accepted 19 June 2019; published online 31 July 2019)

Non-Hermitian parity-time (\mathcal{PT}) symmetric systems that possess real eigenvalues have been intensively investigated in quantum mechanics and rapidly extended to optics and acoustics demonstrating a lot of unconventional wave phenomena. Here, a \mathcal{PT} symmetric metamaterial beam is designed based on shunted piezoelectric patches and asymmetric wave scattering in the form of flexural waves is demonstrated through analytical and numerical approaches. The gain and loss components in the \mathcal{PT} symmetric beam are realized by the introduction of negative and positive resistances into the external shunting circuits, respectively. Effective medium theory and transfer matrix method are employed to determine the effective material parameters and scattering properties of the \mathcal{PT} symmetric metamaterial beam. Unidirectional reflectionlessness has been demonstrated analytically and numerically, together with illustrations of the \mathcal{PT} phase transition and exceptional points. The tunability of exceptional points is studied by changing the spacing between piezoelectric patches and shunting circuit parameters. The design explores complex material parameters of the beam structure, and could open unique ways to asymmetric wave control, enhanced sensing, amplification, and localization of flexural waves.

© 2019 Acoustical Society of America. <https://doi.org/10.1121/1.5116561>

[JFL]

Pages: 850–862

I. INTRODUCTION

Non-Hermitian parity-time (\mathcal{PT}) symmetric systems that possess real spectrums have attracted a great deal of attention and been intensively investigated in quantum mechanics during the past two decades.^{1,2} Exceptional points (EPs) behaving as thresholds of phase transitions are of particular interest. For example, below the EP, the spectrum of the system is real, corresponding to the exact \mathcal{PT} symmetric phase. On the contrary, beyond the EP, the system enters the \mathcal{PT} broken phase where the spectrum becomes complex.¹ Owing to the similarity between Schrödinger and Helmholtz equations, \mathcal{PT} symmetric systems have been recently extensively studied in electromagnetic and acoustic devices,^{3–29} and paved the way to some fascinating and unconventional applications, such as sensors with extremely high sensitivity,^{24,26,27} unidirectional cloaks^{7,20,25} and robust wireless power transfer.²⁸ The key in designing acoustic and optical \mathcal{PT} symmetric devices is to introduce balanced loss and gain components. In other words, the imaginary part of the refractive index is required to be an odd function in space, while the real part is even.^{1–5,7,8,12,14} Based on this strategy, many interesting and unconventional wave phenomena have been demonstrated numerically and/or experimentally in optics and acoustics, such as asymmetric scattering,^{3–5,7,9,11,12,14,16} negative refraction^{18,19} and coherent perfect absorber and laser.^{21–23}

Metamaterials are artificial structures with periodically or non-periodically arranged subwavelength units, which exhibit unusual properties beyond naturally occurring materials,^{29–41}

providing an appealing solution to achieving loss and gain mediums for \mathcal{PT} symmetric devices. In order to realize optical loss and gain components, active materials such as Fe-doped LiNbO_3 and InGaAsP have been utilized.^{4,15} In acoustics, leaky waveguides with multiple slits and active microphone arrays have been designed to access loss and gain.¹⁴ In practice, gain components usually require active approaches, resulting in complex control systems. To circumvent this complexity, quasi- \mathcal{PT} symmetric devices containing only passive loss components have been proposed. Even though those systems are not strictly \mathcal{PT} symmetric, similar acoustic and optical asymmetric scattering phenomena can still be observed.^{4,5,11,16}

Nevertheless, the study on non-Hermitian \mathcal{PT} symmetry for elastic waves in solid media is still in the early stage. Piezoelectric materials have been regarded as one of the best candidates to achieve the elastic gain and loss because the energy conversion between mechanical and electrical domains can be controlled by electrical circuits in real-time.^{33,37,41–51} Piezotronics effect in piezoelectric semiconductors was first utilized to amplify and attenuate pressure waves in the \mathcal{PT} symmetric elastic system, where the asymmetric scattering (or unidirectional reflectionlessness) has been proposed theoretically.¹⁷ On the other hand, electrical-circuit-shunted piezoelectric ceramic materials have been extensively applied in vibration and wave attenuation applications for decades, where elastic energy can be transferred and absorbed by the shunted resistance.^{42–51} Very recently, a tunable \mathcal{PT} symmetric elastic system with shunted piezoelectric materials has been investigated analytically for pressure waves.⁴² With the help of the negative and positive shunting resistances together with inductance, balanced gain and loss can be built.

^{a)}Electronic mail: huangg@missouri.edu

Here, we explore the \mathcal{PT} symmetry in an elastic beam for flexural waves based on shunted piezoelectric patches. We first prove the \mathcal{PT} symmetry condition for flexural waves, based on Euler's assumptions, also requires the balanced gain and loss. They are then realized with shunted negative and positive resistances, respectively, together with a negative capacitance. In particular, two analytical approaches, effective medium theory and transfer matrix method, are employed to determine effective material parameters and asymmetric scattering properties of the \mathcal{PT} symmetric metamaterial beam. Numerical simulations are carried out to validate analytical predictions and demonstrate the asymmetric scattering phenomena. We also show that the unidirectional reflectionlessness originates from the \mathcal{PT} phase transition or EPs. Furthermore, tunability of the EP is examined through selecting different spacing between piezoelectric patches and shunting circuit parameters. The design expands material parameters governing the propagation of flexural waves to the complex domain, and explores the asymmetric flexural wave scattering originating from the \mathcal{PT} symmetry. This could open new pathways to applications such as asymmetric control, enhanced sensing, amplification and localization of flexural waves.

II. DESIGN AND ANALYSIS FOR \mathcal{PT} SYMMETRIC METAMATERIAL BEAM

A. \mathcal{PT} symmetry condition for flexural waves

To examine the exact \mathcal{PT} symmetry condition for flexural waves propagating in the x -direction along a one dimensional (1D) thin beam, we consider Euler beam assumptions and the governing equation is written as

$$\frac{\partial^2}{\partial x^2} \left(D_{eff}(x) \frac{\partial^2 w(x)}{\partial x^2} \right) + \rho_{eff}(x) h_b \frac{\partial^2 w(x)}{\partial t^2} = 0, \quad (1)$$

where $w(x)$, $D_{eff}(x)$, $\rho_{eff}(x)$ and h_b denote the displacement field of the flexural wave, effective bending stiffness, effective mass density and thickness of the thin beam. \mathcal{PT} symmetry of Eq. (1) implies

$$\begin{aligned} & \hat{\mathcal{P}}\hat{\mathcal{T}} \left\{ \frac{\partial^2}{\partial x^2} \left(D_{eff}(x) \frac{\partial^2 w(x)}{\partial x^2} \right) + \rho_{eff}(x) h_b \frac{\partial^2 w(x)}{\partial t^2} \right\} \\ &= \frac{\partial^2}{\partial x^2} \left(D_{eff}^*(-x) \frac{\partial^2 \hat{\mathcal{P}}\hat{\mathcal{T}}\{w(x)\}}{\partial x^2} \right) \\ &+ \rho_{eff}^*(-x) h_b \frac{\partial^2 \hat{\mathcal{P}}\hat{\mathcal{T}}\{w(x)\}}{\partial t^2}, \end{aligned} \quad (2)$$

where $\hat{\mathcal{P}}$ and $\hat{\mathcal{T}}$ are the parity and time reversal operators, respectively.

Performing \mathcal{PT} transformations in Eq. (2), the \mathcal{PT} symmetry condition can be simply derived as

$$D_{eff}(x) = D_{eff}^*(-x), \quad \rho_{eff}(x) = \rho_{eff}^*(-x), \quad (3)$$

indicating that loss and gain of flexural waves should be balanced in space.

B. Design principles

Based on the condition illustrated in Eq. (3), Fig. 1(a) shows the schematic of a \mathcal{PT} symmetric beam for asymmetric scattering of flexural waves, where discrete loss and gain components are distributed along the beam in a manner that follows an odd function respect to a point. Without loss of generality, ρ_{eff} is assumed as real values in the study. We focus on the physical realization of the complex effective bending stiffness to induce the loss and gain of flexural waves. For this purpose, two piezoelectric patches are bonded onto a host beam and each patch is shunted with a negative or positive resistant, (R_{sh} or $-R_{sh}$), and a negative capacitor C_{sh} connected in parallel [Fig. 1(b)]. In particular, the negative resistance, $-R_{sh}$, aims to comprise the gain component, whereas the positive resistance, R_{sh} , aims to constitute the loss component. The negative capacitance⁵¹ is mainly responsible for amplifying the gain and loss effects and, at the same time, tuning the storage modulus. In general, both negative resistance and negative capacitance can be physically attained by negative impedance converters (non-Foster circuits) [insets of Fig. 1(b)]. The resulted effective negative impedance can be analytically determined,

$$Z_{eff} = -Z, \quad (4)$$

where Z denotes a positive electric impedance element. In our design, Z is a positive resistance R_{sh} or a positive capacitance C_0 for the realization of a negative resistance $-R_{sh}$ or a negative capacitance $C_{sh} = -C_0$, as illustrated by the insets of Fig. 1(b).

Note that the negative capacitance is technically not equivalent to the inductance.⁴² Adding inductance to the shunting circuit will produce electrical resonance, which makes the resulted effective parameters and its related wave behavior highly frequency-dependent. On the other hand, using negative capacitance can prevent the frequency-dependency and achieve exceptional points at multiple frequencies in the \mathcal{PT} symmetric beam. Since gain and loss components are purely controlled by shunting circuit parameters, the system designed possesses a huge potential for real-time and remote tuning of asymmetric scattering of flexural waves.

C. Analytical characterizations of the \mathcal{PT} symmetric metamaterial beam

To characterize the asymmetric scattering of flexural waves with the \mathcal{PT} symmetric metamaterial beam with shunted piezoelectric patches, the scattering matrix of a finite \mathcal{PT} symmetric metamaterial beam is derived first based on the transfer matrix method (TMM) and its effective material parameters is then retrieved using the effective medium theory (EMT).

Plane stress assumptions are considered in the study. For the unit cell structure shown in Fig. 2(a), thicknesses and lengths of the host beam and piezoelectric patches are denoted as h_b , h_p , and L_b , respectively. The shunting impedance is represented by Z_{sh} . Considering traction-free boundary conditions on top and bottom surfaces of the metamaterial beam, linear constitutive relations of piezoelectric patches can be simplified and written as^{37,41,44}

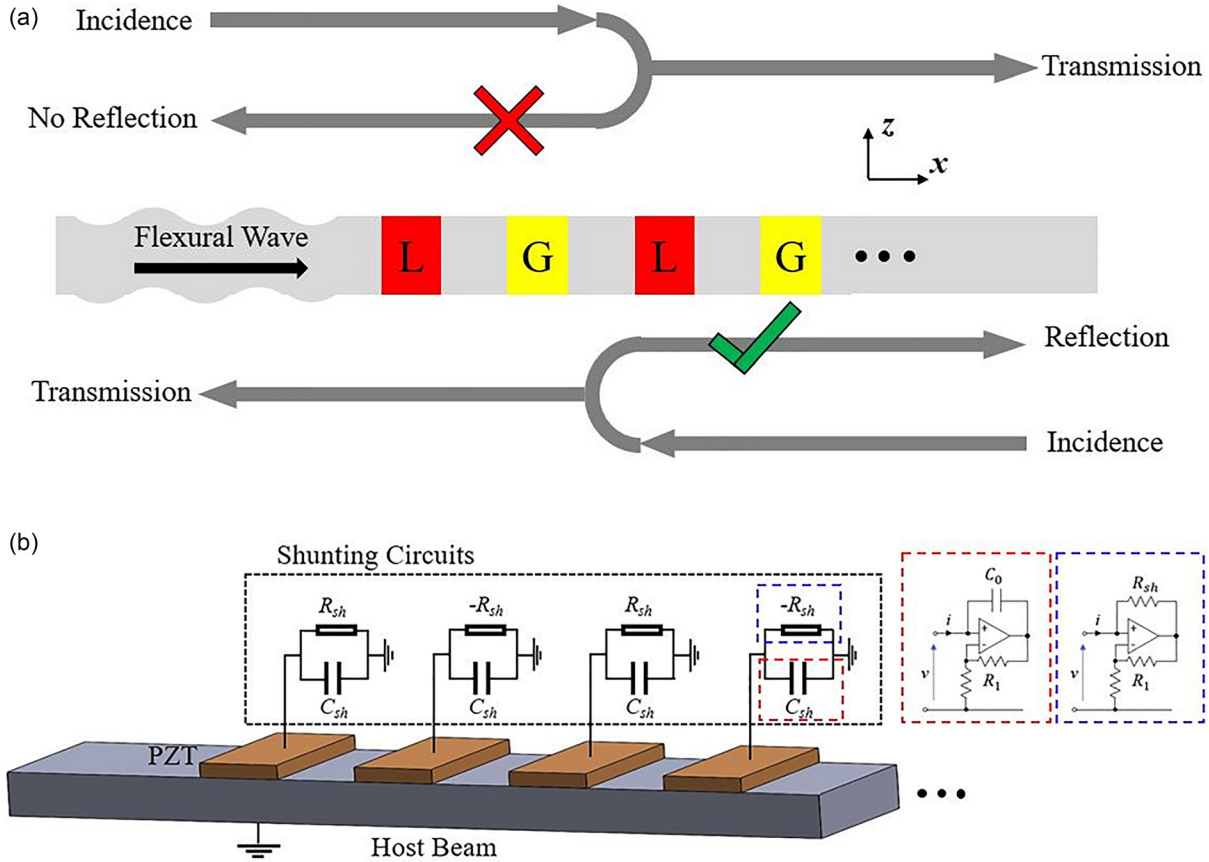


FIG. 1. (Color online) (a) Schematic of the non-Hermitian \mathcal{PT} symmetric beam for asymmetric flexural wave scattering. Unidirectional reflectionlessness is illustrated in the figure. (b) Physical realization of the \mathcal{PT} symmetric beam with piezoelectric patches shunted with negative and positive resistances together with a negative capacitance connected in parallel. The insets highlighted in red and blue illustrate the physical realization of the electrical shunting components.

$$S_1 = s_{11}^E T_1 + d_{31} E_3, \quad (5a)$$

$$D_3 = d_{31} T_1 + \epsilon_{33}^T E_3, \quad (5b)$$

where S_1 and T_1 represent the normal strain and stress along the x -direction, respectively, and D_3 , and E_3 represent the electric displacement and electric field along the z -direction, respectively. s_{11}^E , d_{31} , and ϵ_{33}^T are the compliance coefficient under constant electric field, dielectric constant under constant stress and piezoelectric coefficient, respectively. For the unit cell shown in Fig. 2(a), the displacement field along the x -direction, u , can be assumed as the combination of the displacements at the mid-plane of the host beam in the form of

$$u(x, z) = u_0(x) - z \frac{\partial w}{\partial x}, \quad (6)$$

where u_0 represent the displacement along the x -direction.

A linear electric field distribution and its corresponding electric potential are assumed as

$$E_3(x, z) = z \cdot a(x) + b(x), \quad (7a)$$

$$V(x, z) = - \left[\frac{a(x)}{2} z^2 + b(x)z + c(x) \right], \quad (7b)$$

where a , b , and c are the distribution functions which can be obtained through piezoelectric governing equations and electric boundary conditions.

By combining Eqs. (5), (6), and (7a) and considering the electrical governing equation $\partial D_3 / \partial z = 0$, the distribution functions a , b , and c , and the electric potential on the upper electrode V_{upper} can be determined, respectively, as³⁷

$$a = \frac{d_{31}}{s_{11}^E \epsilon_{33}^T - d_{31}^2} \frac{\partial^2 w}{\partial x^2}, \quad (8a)$$

$$b = - \frac{V_{upper}}{h_p} - \frac{a}{2} (h_b + h_p), \quad (8b)$$

$$c = - \frac{h_b^2}{8} a - \frac{h_b}{2} b, \quad (8c)$$

$$V_{upper} = \frac{i\omega \frac{d_{31}}{s_{11}^E} Z_{sh} \int_0^{L_b} \left(\frac{\partial u_0}{\partial x} - \frac{h_p + h_b}{2} \frac{\partial^2 w}{\partial x^2} \right) dx}{1 + i\omega C_p^T (1 - k_{31}^2) Z_{sh}}, \quad (8d)$$

where $k_{31}^2 = d_{31}^2 / s_{11}^E \epsilon_{33}^T$ is the electro-mechanical coupling coefficient and the capacitance of the piezoelectric patch, $C_p^T = \epsilon_{33}^T L_b / h_p$.

Integrating stress components over the thickness of the beam with respect to the mid-plane in the host beam, the bending moment, normal and shear forces in the unit cell can be obtained as

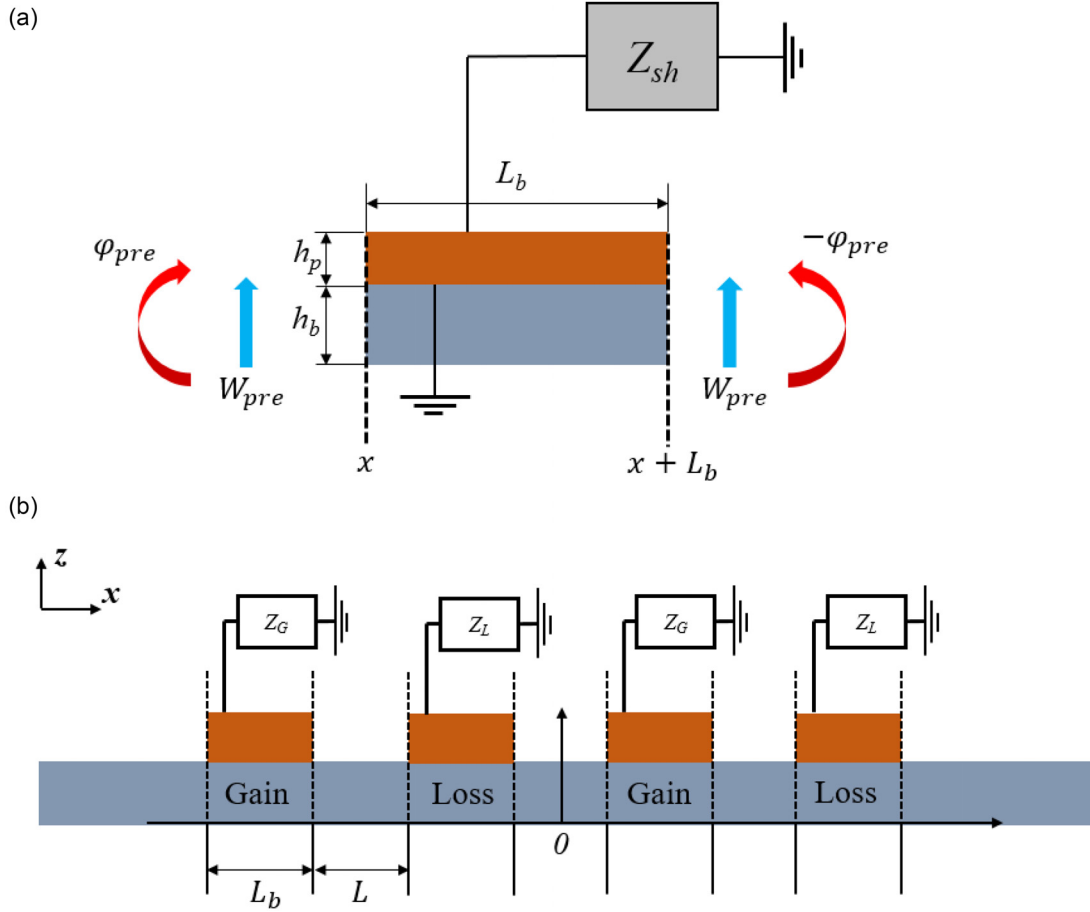


FIG. 2. (Color online) (a) Loss or gain unit cell used in effective medium theory and transfer matrix method. (b) Schematic of the \mathcal{PT} symmetric metamaterial beam used in transfer matrix method.

$$M = I \frac{\partial^2 w}{\partial x^2} - J \frac{\partial u_0}{\partial x} - FV_{upper}, \quad (9a)$$

$$N = K \frac{\partial u_0}{\partial x} - J \frac{\partial^2 w}{\partial x^2} + GV_{upper}, \quad (9b)$$

$$T = I \frac{\partial^3 w}{\partial x^3} - J \frac{\partial^2 u_0}{\partial x^2}, \quad (9c)$$

where

$$I = \frac{Eh_b^3}{12} + \frac{6h_b h_p^2 + 3h_b^2 h_p + 4h_p^3}{12s_{11}^E} + \frac{h_p^3 d_{31}^2}{12s_{11}^E (s_{11}^E \varepsilon_{33}^T - d_{31}^2)},$$

$$J = \frac{h_p^2 + h_b h_p}{2s_{11}^E}, \quad K = Eh_b + \frac{h_p}{s_{11}^E}, \quad F = \frac{(h_b + h_p)d_{31}}{2s_{11}^E},$$

$$G = \frac{d_{31}}{s_{11}^E},$$

and E denotes the Young's modulus of the host beam.

Based on Eq. (9), equations of motion for coupled flexural and longitudinal waves are derived as

$$I \frac{\partial^4 w}{\partial x^4} - J \frac{\partial^3 u_0}{\partial x^3} + \bar{\rho} \frac{\partial^2 w}{\partial t^2} = 0, \quad (10a)$$

$$K \frac{\partial^2 u_0}{\partial x^2} - J \frac{\partial^3 w}{\partial x^3} - \bar{\rho} \frac{\partial^2 u_0}{\partial t^2} = 0, \quad (10b)$$

in which $\bar{\rho} = \rho_b h_b + \rho_p h_p$. Here ρ_b and ρ_p are the mass density of the support beam and the piezoelectric material, which are given in Table I.

General solutions to Eq. (10) can be found as

$$u_0 = \sum_{n=1}^6 \bar{A}_n \beta_n e^{\gamma_n x}, \quad (11a)$$

$$w = \sum_{n=1}^6 \bar{A}_n e^{\gamma_n x}, \quad (11b)$$

where \bar{A}_n are arbitrary constants, γ_n are the roots of the characteristic equations given by Eq. (10) and $\beta_n = (I\gamma_n^4 - \omega^2 \bar{\rho}) / (J\gamma_n^3)$. Substituting Eq. (11) into Eq. (8d), the

TABLE I. Unit cell geometrical and material parameters.

L_b	20 mm	c_{11}^E	126 GPa
E_b	70 GPa	c_{12}^E	79.5 GPa
h_b	1.6 mm	c_{13}^E	84.1 GPa
h_p	0.5 mm	c_{33}^E	117 GPa
ρ_b	2700 kg/m ³	c_{44}^E	23 GPa
ρ_p	7600 kg/m ³	c_{66}^E	23.25 GPa
e_{15}	17 C/m ²	d_{31}	-2.74×10^{-12}
e_{31}	-6.55 C/m ²	ε_{11}^S	1700 ε_0
e_{33}	23.3 C/m ²	ε_{33}^S	1470 ε_0
L	200 mm	ε_{33}^T	3443 ε_0

electric potential on the upper electrode of the piezoelectric patch can be rewritten as

$$V_{upper} = \sum_{n=1}^6 \frac{i\omega \frac{d_{31}}{s_{11}^E} Z_{sh} \left(\beta_n - \frac{h_b + h_p}{2} \gamma_n \right) (e^{\gamma_n L_b} - 1)}{1 + i\omega C_p^T (1 - k_{31}^2) Z_{sh}}. \quad (12)$$

Similarly, for host beam sections without piezoelectric patches, longitudinal and flexural wave components are decoupled and can be simply written as

$$u_0^{(b)} = \sum_{n=5}^6 \bar{A}_n^{(b)} e^{\gamma_n^{(b)} x}, \quad (13a)$$

$$w_0^{(b)} = \sum_{n=1}^4 \bar{A}_n^{(b)} e^{\gamma_n^{(b)} x}, \quad (13b)$$

in which $\bar{A}_n^{(b)}$ are arbitrary constants, and

$$\gamma_{1,2}^{(b)} = \pm i \sqrt{\frac{12\rho_b \omega^2}{Eh_b^2}}, \quad \gamma_{3,4}^{(b)} = \pm \sqrt{\frac{12\rho_b \omega^2}{Eh_b^2}}, \quad \text{and}$$

$$\gamma_{5,6}^{(b)} = \pm i \sqrt{\frac{\rho_b \omega^2}{E}}.$$

To construct transfer matrices, a vector $Y_i = [w, \partial w / \partial x, M, T, u_0, N]^T$ is then defined where $i = b$ or p representing host beam sections or shunted piezoelectric beam sections, respectively. With the help of Eqs. (11)–(13), Eq. (9) can be written in the form of

$$Y_p = \mathbf{B}_p A_p, \quad (14a)$$

$$Y_b = \mathbf{B}_b A_b, \quad (14b)$$

where the characteristic matrix \mathbf{B}_i and the vector A_i ($i = b$ or p) representing the complex wave amplitudes are shown in the Appendix.

Based on Eq. (14) and applying continuity boundary conditions, the transfer matrix \mathbf{M}_i of the unit cell, where $i = G$ or L , is derived as

$$A_b(x + L_b) = \mathbf{B}_b^{-1} \mathbf{B}_p(x + L_b) \mathbf{P}_p \mathbf{B}_p^{-1}(x) \mathbf{B}_b A_b(x) = \mathbf{M}_i A_b(x), \quad (15)$$

where \mathbf{P}_p is the propagation matrix of the shunted piezoelectric beam section (Appendix).

Then the global transfer matrix for an array of m unit cells illustrated in Fig. 2(b) then reads

$$\mathbf{M}^{TMM} = (\mathbf{M}_G \mathbf{P}_b^{-1} \mathbf{M}_L \mathbf{P}_b^{-1})^m \quad (16)$$

in which \mathbf{P}_b is the propagation matrix of the host beam sandwiched by the gain and loss sections, and is given in the Appendix. To obtain the scattering matrix, an incident flexural wave with unitary displacement amplitude is prescribed on the left or right background beams as

$$\begin{bmatrix} t_{l(r)} \\ 0 \\ t_{l(r)}^e \\ 0 \\ t_{l(r)}^p \\ 0 \end{bmatrix} = \mathbf{M}_{l(r)}^{TMM} \begin{bmatrix} 1 \\ r_{l(r)} \\ 0 \\ r_{l(r)}^e \\ 0 \\ r_{l(r)}^p \end{bmatrix}, \quad (17)$$

where the subscripts denote the incident direction, and the superscripts “ e ” and “ p ” represent the evanescent flexural and the propagating longitudinal waves, respectively. Here, $\mathbf{M}_l^{TMM} = (\mathbf{M}_G \mathbf{P}_b \mathbf{M}_L \mathbf{P}_b)^m$ for the transmission from the left side, while $\mathbf{M}_r^{TMM} = (\mathbf{M}_L \mathbf{P}_b \mathbf{M}_G \mathbf{P}_b)^m$ for the opposite. Solving the first, second, fourth, and sixth equations involved in Eq. (16) gives the scattering matrix

$$\mathbf{S}^{TMM} = \begin{bmatrix} t_l & r_r \\ r_l & t_r \end{bmatrix}$$

for flexural waves.

Next, we determine the effective mass density ρ_{eff} and effective bending stiffness D_{eff} for the beam section with a shunted piezoelectric patch.³⁷ Note that the size of the unit cell should be sufficiently small compared to the wavelength in order for effective medium theory to work properly. For the unit cell structure shown in Fig. 2(a), the physical quantities on the right edge ($x = L_b$) are related to that on the left edge ($x = 0$) as

$$Y_b(L_b) = \mathbf{T}_{bb} Y_b(0), \quad (18)$$

in which the value of x in the schematic of the unit cell is set to be 0, and the transfer matrix reads

$$\mathbf{T}_{bb} = \mathbf{B}_p(L_b) \mathbf{P}_p \mathbf{B}_p^{-1}(0).$$

To determine the effective mass density, the transverse harmonic displacement field at the left ($x = 0$) and right ($x = L_b$) boundaries of the metamaterial unit cell is prescribed by W_{pr} , where the rotational angle and longitudinal displacement is set to zero at these two boundaries. A commercial finite element software COMSOL Multiphysics is then used to solve the harmonic problem, and the reaction forces are calculated at boundaries. The effective mass density can be determined according to the following expression:

$$\rho_{eff} = \frac{2T^l(0)}{\omega^2 W_{pre} L_b h_b}, \quad (19)$$

where T^l denotes the calculated reaction force at the left edge of the unit cell.

To determine the effective bending stiffness, the harmonic rotational angles at the left ($x = 0$) and right ($x = L_b$) boundaries of the metamaterial unit cell are assumed as $-\varphi_{pr}$ and φ_{pr} , respectively. The transverse displacements are fixed at zero for both the boundaries. We release the longitudinal displacement at the boundaries on either one side

or two sides (the longitudinal force is set to be zero) such that the global reaction bending moments on the boundaries can be naturally obtained with respect to the rotational center, where effects of the longitudinal displacement are decoupled. Specifically, the longitudinal displacement on the left boundary ($x = 0$) of the unit cell is fixed and the longitudinal force on the right boundary ($x = L_b$) is set to be zero, where the obtained reaction bending moment with respect to the rotational center can be used for the effective bending stiffness calculation. After solving the harmonic problem numerically, the effective bending stiffness can be determined according to the following equation:

$$D_{\text{eff}} = \frac{M^{(r)}(L_b)}{2\varphi_{\text{pre}}}, \quad (20)$$

where $M^{(r)}$ represents the reaction bending moment.

The explicit expressions of the effective parameters calculated from matrix operations are too complicated and impractical to be given here. In fact, solving matrix numerically for reaction force T^l and the reaction bending moment $M^{(r)}$ at boundaries of the unit cell is much easier. Note that, in the linear region, those reaction force and reaction bending moment are proportional to W_{pre} and φ_{pre} , respectively. In light of this, effective properties are independent on the prescribed displacement/rotation, which is consistent with the effective medium theory.

In Sec. III, the effective material parameters obtained with the EMT will be compared with the numerically calculated ones for model validations. The results will demonstrate how the shunting circuits can realize desired loss and gain components for flexural waves. After that, the TMM will be used to characterize the scattering properties of the shunted piezoelectric metamaterial beam.

III. RESULTS AND DISCUSSIONS

In the study, the \mathcal{PT} symmetric beam contains piezoelectric patches bonded on an aluminum beam. Half of them are shunted with negative capacitance and negative resistance connected in parallel with the shunting impedance $Z_{sh} = -R_{sh}/(-R_{sh}i\omega C_{sh} + 1)$ to amplify waves, whereas the rest are shunted with negative capacitance and positive resistance connected in parallel with the shunting impedance

$Z_{sh} = R_{sh}/(R_{sh}i\omega C_{sh} + 1)$ to attenuate waves. We define $\alpha_N = C_{sh}/C_T^p$ to represent the shunted negative capacitance. The unit cells are arranged in the fashion that satisfies \mathcal{PT} symmetry condition indicated in Fig. 1.

A. Effective material parameters

To quantitatively characterize the \mathcal{PT} symmetric beam, effective mass density and effective bending stiffness of the shunted piezoelectric beam section are calculated analytically based on Eqs. (19) and (20) and compared with numerical simulations in Fig. 3. Material and geometric parameters used in the study are given in Table I. The negative capacitance ratio α_N and the magnitudes of the positive/negative resistances are chosen to be -0.8 and 1000Ω , respectively. Numerical simulations are conducted with COMSOL Multiphysics, where plane stress assumptions are applied. In the study, we employ a weak formulation on the upper boundary of the piezoelectric patch, where the electrical impedance is shunted. Implementing an external impedance to the electrode on the surface of the piezoelectric patch poses a constrain on the potential and free charge relation

$$\int_{\partial\Omega} \dot{\mathbf{Q}} \cdot \mathbf{n} dA = \frac{V_A}{Z_{sh}}, \quad (21)$$

where \mathbf{Q} and V_A denote the free charge density and the applied potential on the electrode. Therefore, the weak formulation on this boundary reads

$$\int_{\partial\Omega} \delta V_A \mathbf{Q} \cdot \mathbf{n} dA = \frac{\delta V_A V_A}{i\omega Z_{sh}}. \quad (22)$$

As shown in Fig. 3(a), the effective mass densities of the metamaterial beam, ρ_{eff} , with both positive (denoted by ‘‘Loss’’ in the legend) and negative resistances (denoted by ‘‘Gain’’) are the same and nearly constant over the frequencies from 0.1 to 1 kHz. Note that imaginary parts of effective mass densities, ρ_{eff} , are small enough to be negligible. In Figs. 3(b) and 3(c), the normalized effective bending stiffness of the metamaterial beam, D_{eff}/D_b , is shown, where $D_b = E_b h_b^3/12$ is the bending stiffness of the beam section without piezoelectric patch. D_{eff} with positive and negative resistances are conjugate pairs, indicating that the storage

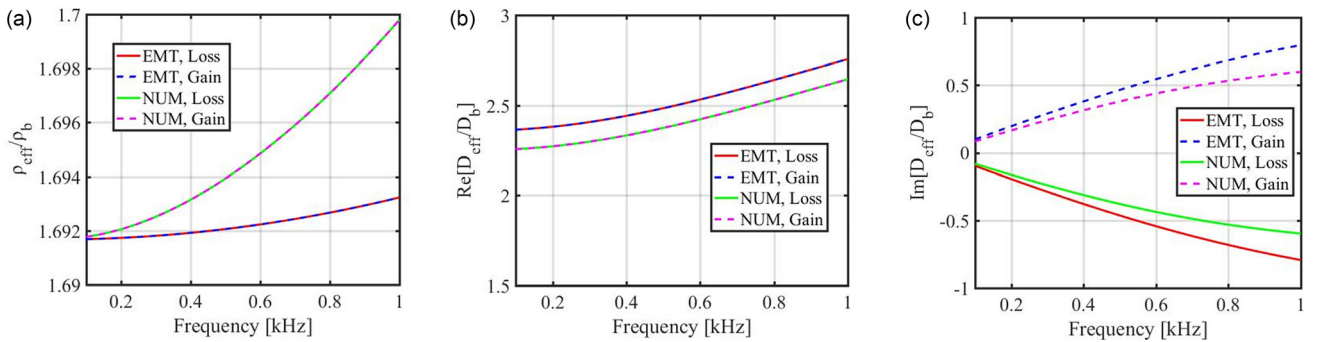


FIG. 3. (Color online) Analytically calculated and numerically simulated effective material parameters: (a) normalized effective mass density ρ_{eff}/ρ_b ; (b), (c) Real (b) and imaginary (c) parts of the normalized effective bending stiffness D_{eff}/D_b . The solid curves correspond to the loss while the dashed to the gain.

stiffnesses are the same, while the loss stiffnesses are opposite, being able to compose balanced loss and gain units required by the flexural wave \mathcal{PT} symmetry condition in Eq. (3). It should be noted that the effective bending stiffness is frequency dependent thanks to the presence of the resistance in the shunting circuits. This can be easily checked with Eq. (12). When only the capacitance appears in Z_{sh} , ω is cancelled. Whereas, in the presence of resistance, ω cannot be cancelled anymore. In particular, the normalized storage stiffnesses are around 2.5 for the frequencies from 0.1 to 1 kHz, and the magnitudes of loss and gain stiffness gradually increase as the frequency increases from 0.1 to 1 kHz. Overall, good agreement between analytical and numerical results is clearly seen, validating the proposed EMT model. Note that small discrepancies of the effective mass density and effective bending stiffness can be attributed to the assumptions used in the analytical model such as linearized displacement and electric fields along the thickness direction.

To further characterize the effective bending stiffness of the metamaterial beam controlled by the shunting circuit, Figs. 4(a) and 4(b) show analytically calculated real and imaginary parts of the normalized effective bending stiffness by continuously changing the negative capacitance and the resistance. In the calculations, the frequency is selected as 0.5 kHz, and other parameters are left unchanged as those in

Fig. 3. Only positive resistance is used for loss characterizations. As illustrated in Figs. 4(a) and 4(b), when R_{sh} is sufficiently small, the shunting circuit is nearly shorted, producing nearly constant bending stiffness with zero loss, no matter what kinds of negative capacitances are used. By gradually increasing R_{sh} , the effects of the negative capacitance become more prominent, i.e., the real part of the bending stiffness can be changed from positive to negative values near $\alpha_N = -0.89$, and the loss is strong, which results in a large material mismatch with respect to the background medium. However, extremely large resistance will suppress the loss properties (not shown in the figure), as an infinitely large impedance will make the circuit open, and only the negative capacitance is left. By changing the frequency to 1 kHz [Figs. 4(c) and 4(d)], both the real and imaginary bending stiffnesses are in the same patterns as those in Figs. 4(a) and 4(b), and only the gradients with respect to the circuit parameters become a little bit larger.

As can be found from Figs. 3 and 4, the requirements on material parameters of the \mathcal{PT} symmetric beam can be fully satisfied by the metamaterial with different shunting circuits, namely positive and negative resistances. In addition, the material parameters, including both the real and imaginary parts, can be flexibly tuned to extremely large regions through the circuit control.

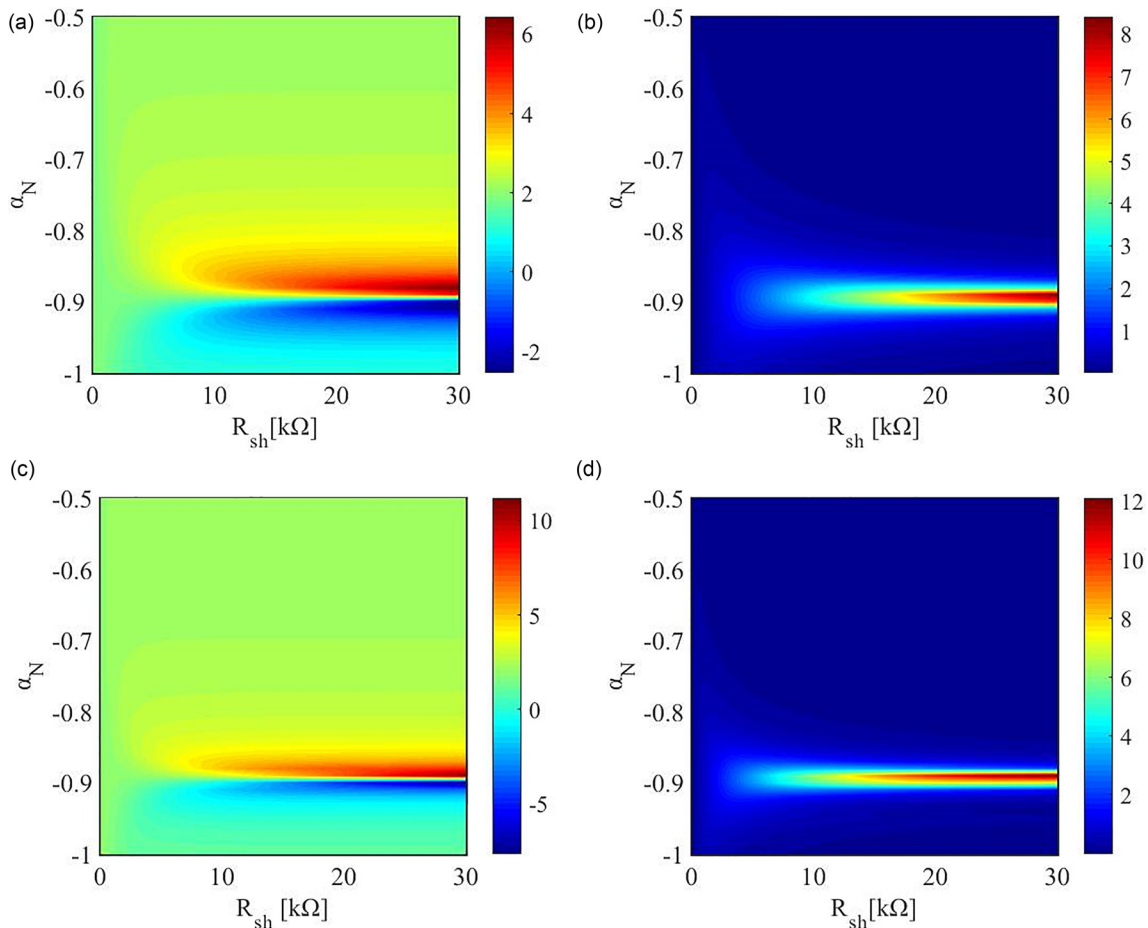


FIG. 4. (Color online) (a), (b) Real (a) and imaginary (b) parts of the effective bending stiffness with continuously changed R_{sh} at 0.5 kHz. (c), (d) Real (c) and imaginary (d) parts of the effective bending stiffness with continuously changed R_{sh} at 1 kHz.

B. Scattering matrix

To characterize wave transmission and reflection properties of the \mathcal{PT} symmetric metamaterial beam, one pair of loss and gain components is first considered and illustrated in Fig. 5(a). The design contains two piezoelectric patches. Each of them is connected with a negative capacitance and a positive/negative resistance in parallel. The transmission and reflection coefficients are calculated analytically and numerically and shown in Figs. 5(b)–5(d). In analytical calculations, the TMM is applied. In numerical simulations, two perfectly matched layers (PMLs) are attached to the two ends of the host beam to suppress boundary reflections, and other boundaries are left free, as shown in the top panel of Fig. 6. To generate propagated flexural waves, a point load is applied on the host beam on the left or right side of the sample. In the study, $L_b = 45$ mm, and the distance between the two patches, L , is selected as 200 mm. Other geometric and material parameters used in the calculations are the same as those used in Fig. 3. The negative capacitance ratio α_N and the magnitudes of the positive/negative resistances are chosen to be -0.855 and 1900Ω , respectively. As shown in Figs. 5(b)–5(d), good agreement can be found between the TMM and numerical simulations. Figure 5(b) shows the amplitude of transmission coefficient $|t|$ for the incidences from the left and right sides of the \mathcal{PT} symmetric beam.

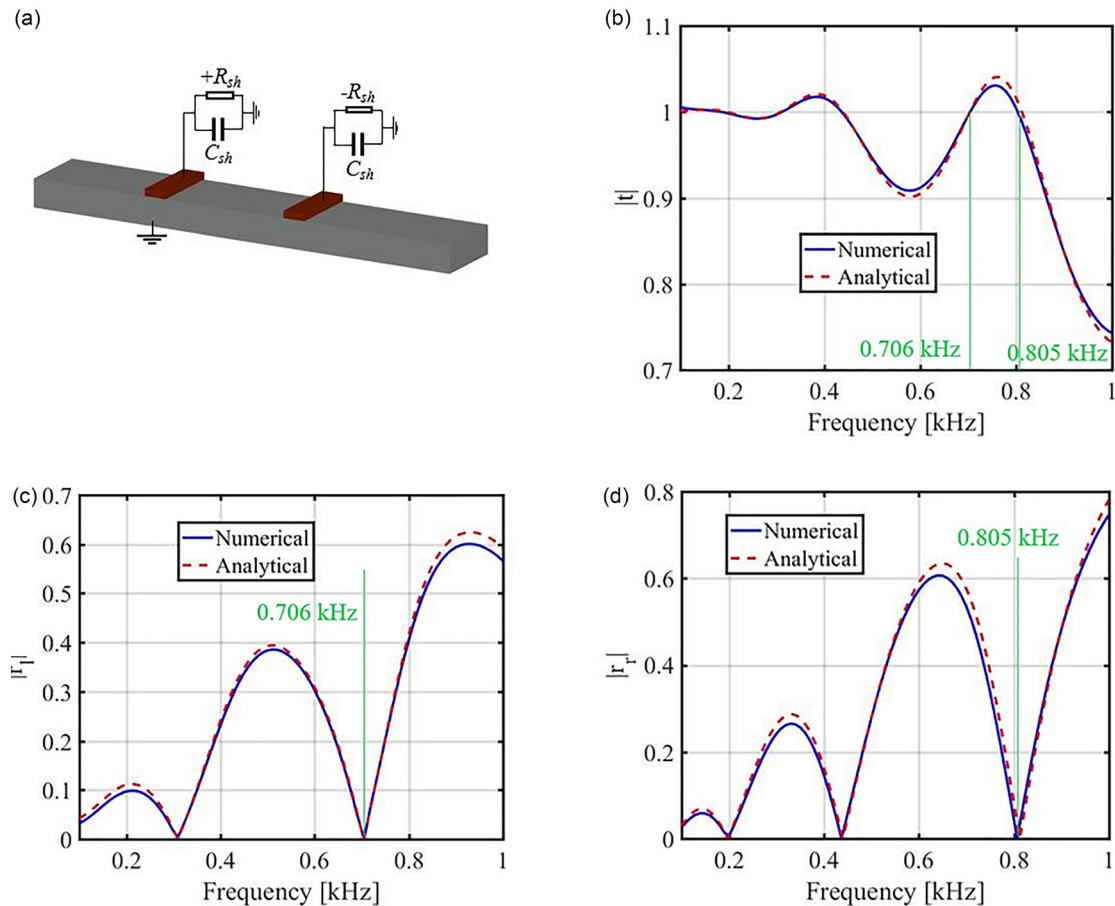


FIG. 5. (Color online) (a) Schematic of the \mathcal{PT} symmetric metamaterial beam with one pair of loss and gain components. (b)–(d) Analytically calculated and numerically simulated amplitudes of transmission (b), left reflection (c) and right reflection (d) coefficients. Two of the unidirectional reflectionlessness points (0.706 and 0.805 kHz) are denoted by green lines.

Since the \mathcal{PT} symmetric beam does not break reciprocity, the transmission coefficients $|t|$ are identical for the two incidences. For the case studied in Fig. 5(a), transmission amplitudes fluctuate around 1 from 0.1 to 1 kHz. It is interesting to note that the reflection coefficients $|r_r|$ and $|r_l|$ for the incidences from the left and right sides of the \mathcal{PT} symmetric beam are asymmetric, i.e., their amplitudes shown in Figs. 5(c) and 5(d) are not equal. In particular, several zero reflection points (dips) are clearly seen in the figures when the flexural wave is incident from one direction, whereas the reflection is non-zero when incident from the other direction, indicating unidirectional reflectionlessness (reflection is zero for the incidence from one side, while the reflection is non-zero when incident from the other side, which is different from the unidirectional transmission). To see the unidirectional reflectionlessness, flexural wave field, $|w|$, from numerical simulations at two of those unidirectional reflectionlessness points (706 and 805 Hz) are presented in Fig. 6. The figures are stretched vertically to help see the field distributions more clearly. As shown in the figures, when the incident frequency is selected at 805 Hz, no reflection is found for the flexural wave incident from the right, whereas the reflection is clearly seen for the flexural wave incident from the left, where interference patterns are produced. However, when the incident frequency is selected at 706 Hz,

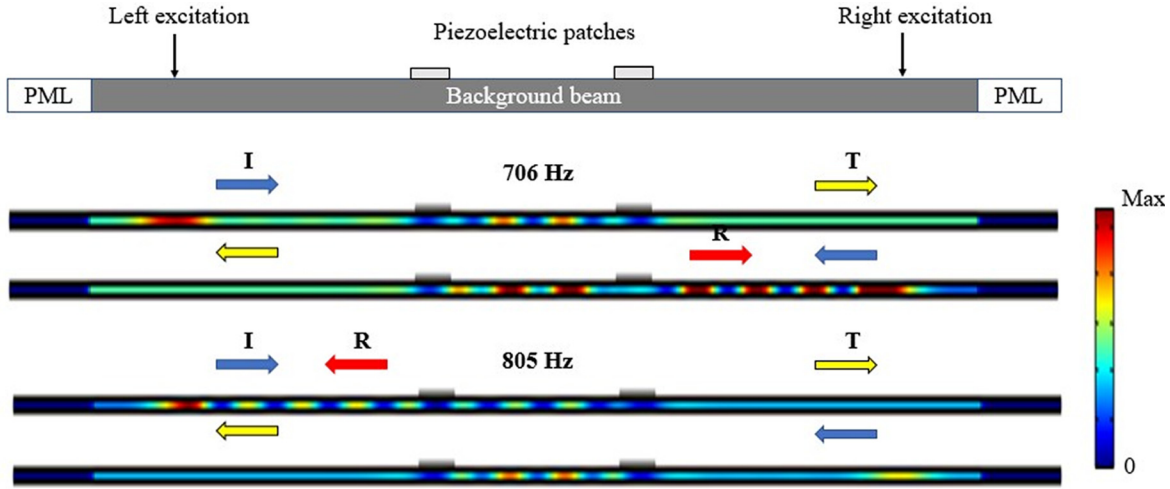


FIG. 6. (Color online) Top: Schematic of the \mathcal{PT} symmetric metamaterial beam in numerical simulations. Bottom: Simulated flexural wave field $|w|$ at two unidirectional reflectionlessness points. The arrows indicate the propagation directions of different wave components. The blue (I), yellow (T), and red (R) arrows correspond to the incidence, transmission, and reflection, respectively.

no reflection is found for the incidence from the left, whereas the reflection is clearly seen for the incidence from the right. Similar wave phenomena can also be found at 202, 310, and 435 Hz, which are not shown in the figure. In addition, it can be found from Fig. 6 that the transmission is unitary at those unidirectional reflectionlessness points (green dashed lines at 706 and 805 Hz), making the \mathcal{PT} symmetric beam perfectly transparent. This property can be applied in designing one-way cloaks of flexural waves.^{7,20,25}

In addition to the unique features in amplitudes of transmission and reflection coefficients, their phase angles also present interesting properties that are shown in Fig. 7. It can be found from the figure that the phase differences between transmission and reflection coefficients are always $\pi/2$, and the two reflection coefficients are either in phase or out of phase. The transition points are exactly at the unidirectional reflectionlessness points in Fig. 5. When the two reflections are in-phase, $|t|$ is less than 1. Whereas, when they are out-of-phase (shaded areas), $|t|$ is greater than 1. To gain more

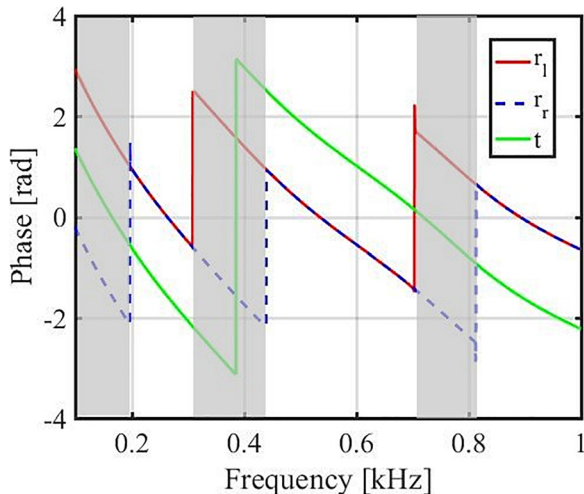


FIG. 7. (Color online) Analytically calculated phase angles of transmission, left reflection and right reflection coefficients.

insights into the transmission and reflection coefficients, the generalized conservation law of the \mathcal{PT} symmetric beam is derived. Thanks to the \mathcal{PT} symmetry, the transfer matrix must satisfy^{22,29}

$$\mathbf{M}^{-1} = \mathbf{M}^*. \quad (23)$$

From Eq. (23), the generalized conservation law can then be derived,²⁹

$$|T - 1| = \sqrt{R_L R_R}, \quad (24)$$

in which $T = |t|^2$, $R_L = |r_l|^2$ and $R_R = |r_r|^2$ denote transmittance, left and right reflectance, respectively. According to Eq. (24), when $T < 1$, $T + \sqrt{R_L R_R} = 1$, the net dissipation or amplification in the \mathcal{PT} symmetric beam is zero, considering the same two incidences from the right and left sides of the \mathcal{PT} symmetric beam. On the other hand, when $T > 1$, the transmitted power is always greater than the input power, and $T - \sqrt{R_L R_R} = 1$. Furthermore, at the unidirectional reflectionlessness points, the transmittance must be equal to 1 [Eq. (24)], which coincides with the findings in Fig. 5. There also exist several points where $R_L = R_R$ accidentally occurs. We notice in Fig. 5 that those points with $R_L = R_R$ can be in regions where $T < 1$ (0.233 and 0.51 kHz) and regions where $T > 1$ (0.375 and 0.766 kHz).

To characterize the properties of \mathcal{PT} symmetric beam, eigenvalues $s_{1,2}$ and corresponding eigenvectors $\bar{S}_{1,2}$ of the scattering matrix are calculated analytically and shown in Fig. 8. Figures 8(a) and 8(b) present amplitudes and phases of the two eigenvalues, respectively. Compare with Fig. 5, when $T < 1$, the amplitudes of the two eigenvalues are unitary [$|s_{1,2}| = 1$ in Fig. 8(a)]. Whereas, when $T > 1$, the amplitude of one of the eigenvalue is less than 1, while the amplitude of the other is greater than 1 (shaded area). It is important to notice that the two eigenvalues coalesce (both the amplitudes and the phases are equal) at the unidirectional reflectionlessness points. In Figs. 8(c)–8(f), the real and imaginary parts of the first and second components of

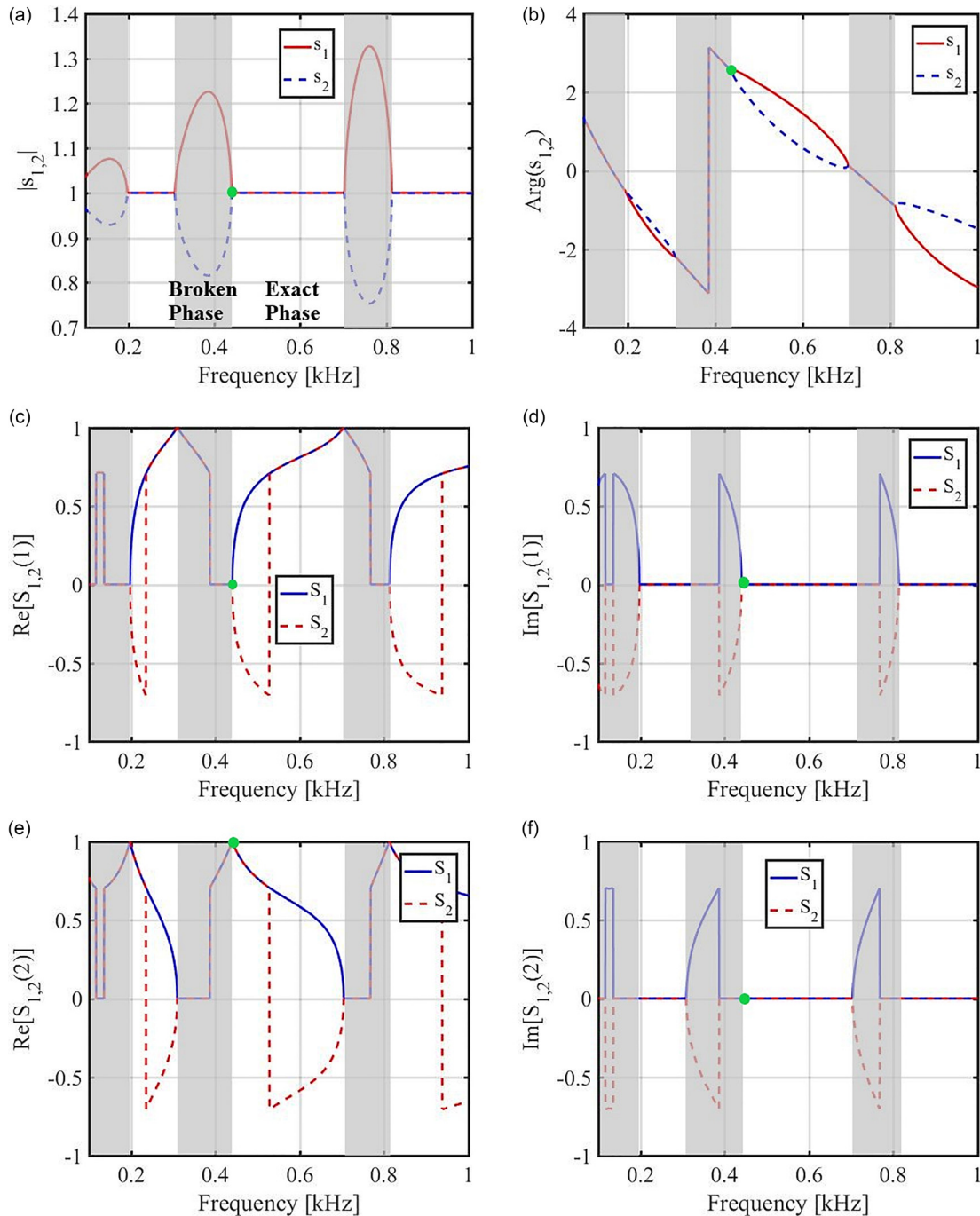


FIG. 8. (Color online) (a), (b) Analytically calculated amplitude (a) and phase (b) of the two eigenvalues. (c), (d) Analytically calculated real (c) and imaginary (d) parts of the first components of the two eigenvectors. (e), (f) Analytically calculated real (e) and imaginary (f) parts of the second components of the two eigenvectors.

the two eigenvectors are shown. At the unidirectional reflectionlessness points, the two eigenvectors coalesce again, indicating that the unidirectional reflectionlessness points of the non-Hermitian \mathcal{PT} symmetric beam are exceptional points (EPs), where only one possible state exists. In addition, when the amplitudes of two eigenvalues are unitary, the two eigenvectors satisfy $\hat{\mathcal{P}}\hat{\mathcal{T}}\bar{s}_{1,2} = \pm\bar{s}_{1,2}$, which corresponds to the \mathcal{PT} exact phase. On the other hand, when the amplitudes of two eigenvalues are not unitary, $\hat{\mathcal{P}}\hat{\mathcal{T}}\bar{s}_{1,2} = \pm\bar{s}_{2,1}$, corresponding to the \mathcal{PT} broken phase. The phase transition points are exactly the EPs or the unidirectional reflectionlessness points.

Furthermore, the unidirectional reflectionlessness observed in Fig. 5 can also be explained by the eigenvectors. For instance, considering the EP at 0.435 kHz [green dots in Figs. 8(c)–8(f)], the first components of the two eigenvectors are zero, indicating that the reflection for the right incidence is zero, which agrees with the reflection coefficients in Fig. 5(d).

C. Tunability of the \mathcal{PT} symmetric metamaterial beam

In this section, we show the tunability of EPs by changing the spacing between the two piezoelectric patches (Fig. 9) and

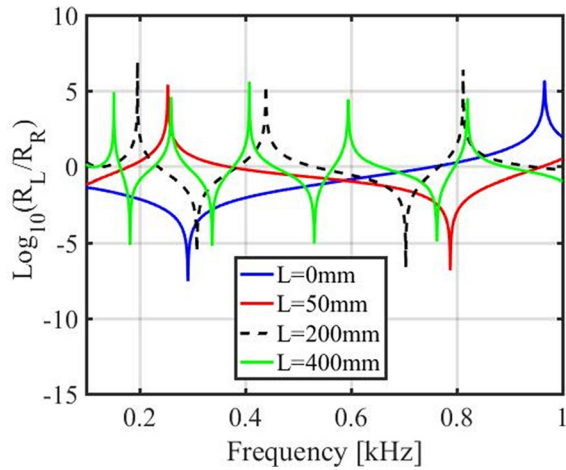


FIG. 9. (Color online) Analytically calculated $\log_{10}(R_L/R_R)$ with different distances separating two piezoelectric patches.

implementing different circuit parameters, i.e., resistance and capacitance (Fig. 10). In the figures, the quantity $\log_{10}(R_L/R_R)$ characterizing the asymmetric reflection is calculated. As a result, small or large values will represent the unidirectional reflectionlessness points or the EPs.

The two reflection coefficients with different distances between the two piezoelectric patches, L , are calculated analytically and shown in Fig. 9. It can be seen that when $L = 0$,

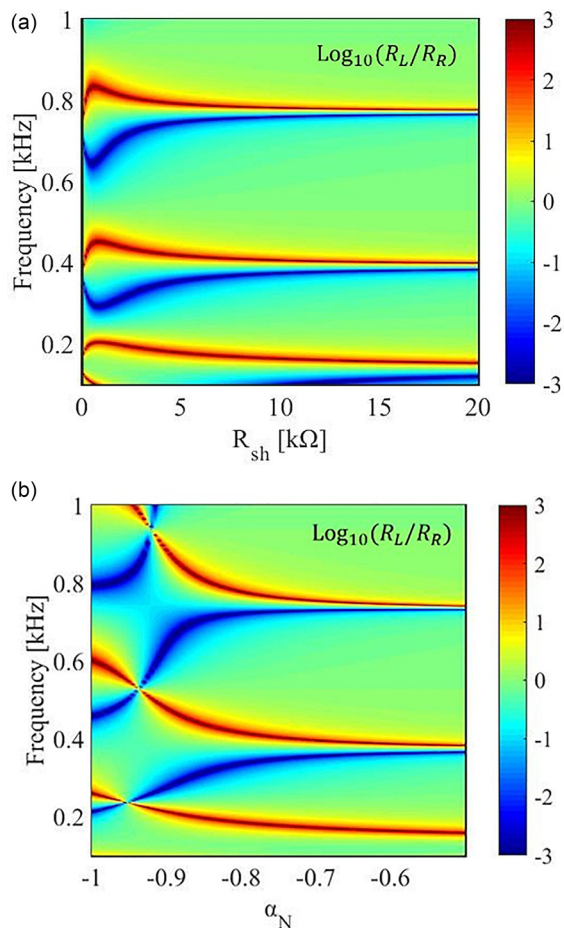


FIG. 10. (Color online) Analytically calculated $\log_{10}(R_L/R_R)$ by continuously changing R_{sh} (a) and α_N (b).

only two EPs (one dip and one peak in the blue curve) are observed at the frequencies between 0.1 and 1 kHz. Increasing L , the frequencies of EPs as well as the frequency difference between EPs are decreased such that the EPs are tuned to different frequencies. Here, the EPs can be regarded as anisotropic transmission resonances with unitary transmission and asymmetric reflection.²⁹ Increasing the length therefore reduces the resonance frequencies. In particular, when $L = 400$ mm, nine EPs are found at the frequencies between 0.1 and 1 kHz.

In Fig. 10, the frequency tunability of the EP is demonstrated by continuously changing the negative capacitance and the negative and positive resistance. Figure 10(a) shows the ratio $\log_{10}(R_L/R_R)$ by continuously increasing R_{sh} , where $\alpha_N = -0.855$. Six EPs are clearly seen, when R_{sh} is less than 7 k Ω . By increasing R_{sh} , the frequencies of the two EPs near 400 and 800 Hz diverge and then become gradually closer. A new EP emerges between the other two EPs near 200 Hz, when R_{sh} is greater than 7 k Ω . The frequency tunability become negligible for R_{sh} greater than 7 k Ω . In Fig. 10(b), R_{sh} is selected as 10 k Ω , and α_N is modulated from -1 to -0.5 . As shown in the figure, when α_N is less than -0.8 , the EPs can be tuned across nearly the entire frequency range of interest. Whereas, with α_N greater than -0.8 , they become convergent and lack tunability, which is due to the small variation of the modulus within this range. Note that the two kinds of EPs cross around $\alpha_N = -0.92$, where the modulus has a pole with changes to the negative capacitance. Based on the results demonstrated in Fig. (10), both the frequency and reflection bias ratio of EPs can be flexibly tailored by properly selecting the shunting circuit parameters.

IV. CONCLUSION

In conclusion, we propose a non-Hermitian \mathcal{PT} symmetric beam based on shunted piezoelectric patches. The realization of gain and loss components relies on the introduction of negative and positive resistances and the negative capacitance into external shunting circuits. Asymmetric flexural wave scattering is investigated analytically and numerically with the focus on the unidirectional reflectionlessness. The scattering matrix and its eigenvalues and eigenvectors are studied in detail for the analyses of exact and broken \mathcal{PT} phases. EPs are then identified at the unidirectional reflectionlessness points. Last, the tunable EPs are demonstrated through varying the spacing between the piezoelectric patches and the shunting circuit parameters. This design could be promising in various applications, such as asymmetric wave control, enhanced sensing, amplification, and localization of flexural waves.

ACKNOWLEDGMENTS

This work is supported by the Air Force Office of Scientific Research under Grant No. AF 9550-18-1-0342 with Program Manager Dr. Byung-Lip (Les) Lee and the NSF EFRI under Award No. 1641078.

APPENDIX

Some of the matrices and vectors in the theoretical section of the main text are shown below in detail:

$$\mathbf{B}_p(x) = \begin{bmatrix} a_{11} & a_{12} & a_{13} & a_{14} & a_{15} & a_{16} \\ a_{21} & a_{22} & a_{23} & a_{24} & a_{25} & a_{26} \\ a_{31} & a_{32} & a_{33} & a_{34} & a_{35} & a_{36} \\ a_{41} & a_{42} & a_{43} & a_{44} & a_{45} & a_{46} \\ a_{51} & a_{52} & a_{53} & a_{54} & a_{55} & a_{56} \\ a_{61} & a_{62} & a_{63} & a_{64} & a_{65} & a_{66} \end{bmatrix}, \quad (\text{A1})$$

where

$$\begin{aligned} a_{1n} &= 1, \\ a_{2n} &= \gamma_n, \\ a_{3n} &= I\gamma_n^2 - J\beta_n\gamma_n - FV_{upper}e^{-\gamma_n x}, \\ a_{4n} &= I\gamma_n^3 - J\beta_n\gamma_n^2, \\ a_{5n} &= \beta_n, \\ a_{6n} &= K\beta_n\gamma_n - J\gamma_n^2 + GV_{upper}e^{-\gamma_n x}. \end{aligned}$$

In Eq. (15), \mathbf{B}_b reads

$$\mathbf{B}_b = \begin{bmatrix} 1 & 1 & 1 & 1 & 0 & 0 \\ \gamma_1^b & \gamma_2^b & \gamma_3^b & \gamma_4^b & 0 & 0 \\ Eh_b^3(\gamma_1^b)^2/12 & Eh_b^3(\gamma_2^b)^2/12 & Eh_b^3(\gamma_3^b)^2/12 & Eh_b^3(\gamma_4^b)^2/12 & 0 & 0 \\ Eh_b^3(\gamma_1^b)^3/12 & Eh_b^3(\gamma_2^b)^3/12 & Eh_b^3(\gamma_3^b)^3/12 & Eh_b^3(\gamma_4^b)^3/12 & 0 & 0 \\ 0 & 0 & 0 & 0 & 1 & 1 \\ 0 & 0 & 0 & 0 & Eh_b\gamma_5^b & Eh_b\gamma_6^b \end{bmatrix}, \quad (\text{A2})$$

$$\mathbf{A}_p = [\bar{A}_1 e^{\gamma_1 x}, \bar{A}_2 e^{\gamma_2 x}, \bar{A}_3 e^{\gamma_3 x}, \bar{A}_4 e^{\gamma_4 x}, \bar{A}_5 e^{\gamma_5 x}, \bar{A}_6 e^{\gamma_6 x}]^T. \quad (\text{A3})$$

$$\mathbf{A}_b = [\bar{A}_{1b} e^{\gamma_1^{(b)} x}, \bar{A}_{2b} e^{\gamma_2^{(b)} x}, \bar{A}_{3b} e^{\gamma_3^{(b)} x}, \bar{A}_{4b} e^{\gamma_4^{(b)} x}, \bar{A}_{5b} e^{\gamma_5^{(b)} x}, \bar{A}_{6b} e^{\gamma_6^{(b)} x}]^T. \quad (\text{A4})$$

In Eqs. (16) and (17), the propagation matrices are defined as

$$\mathbf{P}_p = \begin{bmatrix} e^{\gamma_1 L b} & & & & & \\ & e^{\gamma_2 L b} & & & & \\ & & e^{\gamma_3 L b} & & & \\ & & & e^{\gamma_4 L b} & & \\ & & & & e^{\gamma_5 L b} & \\ & & & & & e^{\gamma_6 L b} \end{bmatrix}, \quad (\text{A5})$$

$$\mathbf{P}_b = \begin{bmatrix} e^{\gamma_1^b L} & & & & & \\ & e^{\gamma_2^b L} & & & & \\ & & e^{\gamma_3^b L} & & & \\ & & & e^{\gamma_4^b L} & & \\ & & & & e^{\gamma_5^b L} & \\ & & & & & e^{\gamma_6^b L} \end{bmatrix}. \quad (\text{A6})$$

¹C. M. Bender and S. Boettcher, "Real spectra in non-Hermitian Hamiltonians having PT symmetry," *Phys. Rev. Lett.* **80**, 5243–5246 (1998).

²C. M. Bender "Making sense of non-Hermitian Hamiltonians," *Rep. Prog. Phys.* **70**(6), 947–1018 (2007).

³C. E. Ruter, K. G. Makris, R. El-Ganainy, D. N. Christodoulides, M. Segev, and D. Kip, "Observation of parity–time symmetry in optics," *Nat. Phys.* **6**, 192–195 (2010).

⁴A. Guo, G. J. Salamo, D. Duchesne, R. Morandotti, M. Volatier-Ravat, V. Aimez, G. A. Siviloglou, and D. N. Christodoulides, "Observation of PT-symmetry breaking in complex optical potentials," *Phys. Rev. Lett.* **103**, 093902 (2009).

⁵Y. Aurégan and V. Pagneux, "PT-symmetric scattering in flow duct acoustics," *Phys. Rev. Lett.* **118**, 174301 (2017).

⁶K. G. Makris, R. El-Ganainy, and D. N. Christodoulides, "Beam dynamics in PT symmetric optical lattices," *Phys. Rev. Lett.* **100**, 103904 (2008).

⁷Z. Lin, H. Ramezani, T. Eichelkraut, T. Kottos, H. Cao, and D. N. Christodoulides, "Unidirectional invisibility induced by PT-symmetric periodic structures," *Phys. Rev. Lett.* **106**, 213901 (2011).

⁸S. V. Dmitriev, A. A. Sukhorukov, and Y. S. Kivshar, "Binary parity-time-symmetric nonlinear lattices with balanced gain and loss," *Opt. Lett.* **35**, 2976–2978 (2010).

⁹B. Peng, S. K. Özdemir, S. Rotter, H. Yilmaz, M. Liertzer, F. Monifi, C. M. Bender, F. Nori, and L. Yang, "Loss induced suppression and revival of lasing," *Science* **346**, 328–332 (2014).

¹⁰R. El-Ganainy, K. G. Makris, D. N. Christodoulides, and Z. H. Musslimani, "Theory of coupled optical PT-symmetric structures," *Opt. Lett.* **32**, 2632–2634 (2007).

¹¹L. Feng, Y.-L. Xu, William S. Fegadolli, Ming-Hui Lu, José E. B. Oliveira, V. R. Almeida, Y.-F. Chen, and A. Scherer, "Experimental demonstration of a unidirectional reflectionless parity-time metamaterial at optical frequencies," *Nat. Mater.* **12**, 108–113 (2013).

¹²X. Zhu, H. Ramezani, C. Shi, J. Zhu, and X. Zhang, "PT-symmetric acoustics," *Phys. Rev. X* **4**, 031042 (2014).

¹³K. Ding, G. Ma, M. Xiao, Z. Q. Zhang, and C. T. Chan, "Emergence, coalescence, and topological properties of multiple exceptional points and their experimental realization," *Phys. Rev. X* **6**, 021007 (2016).

¹⁴C. Shi, M. Dubois, Y. Chen, L. Cheng, H. Ramezani, Y. Wang, and X. Zhang, "Accessing the exceptional points of parity time symmetric acoustics," *Nat. Commun.* **7**, 11110 (2016).

¹⁵F. Liang, Z. J. Wong, R. M. Ma, Y. Wang, and X. Zhang, "Single-mode laser by parity-time symmetry breaking," *Science* **346**, 972–975 (2014).

- ¹⁶T. Liu, X. Zhu, F. Chen, S. Liang, and J. Zhu, “Unidirectional wave vector manipulation in two-dimensional space with an all passive acoustic parity-time-symmetric metamaterials crystal,” *Phys. Rev. Lett.* **120**, 124502 (2018).
- ¹⁷J. Christenson, M. Willatzen, V. R. Velasco, and M. H. Lu, “Parity-time synthetic phononic media,” *Phys. Rev. Lett.* **116**, 207601 (2016).
- ¹⁸R. Fleury, D. L. Sounas, and A. Alù, “Negative refraction and planar focusing based on parity-time symmetric metasurfaces,” *Phys. Rev. Lett.* **113**, 023903 (2014).
- ¹⁹J. Luo, J. Li, and Y. Lai, “Electromagnetic impurity-immunity induced by parity-time symmetry,” *Phys. Rev. X* **8**, 031035 (2018).
- ²⁰X. Zhu, L. Feng, P. Zhang, X. Yin, and X. Zhang, “One-way invisible cloak using parity-time symmetric transformation optics,” *Opt. Lett.* **38**, 2821–2824 (2013).
- ²¹Y. D. Chong, Li Ge, and A. D. Stone, “PT-symmetry breaking and laser-absorber modes in optical scattering systems,” *Phys. Rev. Lett.* **106**, 093902 (2011).
- ²²S. Longhi, “PT-symmetric laser absorber,” *Phys. Rev. A* **82**, 031801(R) (2010).
- ²³Z. J. Wong, Y.-L. Xu, J. Kim, K. O’Brien, Y. Wang, L. Feng, and X. Zhang, “Lasing and anti-lasing in a single cavity,” *Nat. Photon.* **10**, 796–801 (2016).
- ²⁴J. Wiersig, “Sensors operating at exceptional points: General theory,” *Phys. Rev. A* **93**, 033809 (2016).
- ²⁵R. Fleury, D. Sounas, and A. Alu, “An invisible acoustic sensor based on parity-time symmetry,” *Nat. Commun.* **6**, 5905 (2015).
- ²⁶M. Sakhdari, M. Farhat, and P.-Y. Chen, “PT-symmetric metasurfaces: Wave manipulation and sensing using singular points,” *New J. Phys.* **19**, 065002 (2017).
- ²⁷P.-Y. Chen, M. Sakhdari, M. Hajizadegan, Q. Cui, M. M.-C. Cheng, R. El Ganainy, and A. Alù, “Generalized parity–time symmetry condition for enhanced sensor telemetry,” *Nat. Electron.* **1**, 297–304 (2018).
- ²⁸S. Assaworarith, X. Yu, and S. Fan, “Robust wireless power transfer using a nonlinear parity–time-symmetric circuit,” *Nature* **546**, 387–390 (2017).
- ²⁹L. Ge, Y. D. Chong, and A. D. Stone, “Conservation relations and anisotropic transmission resonances in one-dimensional PT-symmetric photonic heterostructures,” *Phys. Rev. A* **85**, 023802 (2012).
- ³⁰J. B. Pendry, “Negative refraction makes a perfect lens,” *Phys. Rev. Lett.* **85**, 3966–3969 (2000).
- ³¹D. R. Smith and N. Kroll, “Negative refractive index in left-handed materials,” *Phys. Rev. Lett.* **85**, 2933–2936 (2000).
- ³²D. R. Smith, W. J. Padilla, D. C. Vier, S. C. Nemat-Nasser, and S. Schultz, “Composite medium with simultaneously negative permeability and permittivity,” *Phys. Rev. Lett.* **84**, 4184–4187 (2000).
- ³³X. P. Li, Y. Y. Chen, G. K. Hu, and G. L. Huang, “A self-adaptive metamaterial beam with digitally controlled resonators for subwavelength broadband flexural wave attenuation,” *Smart Mater. Struct.* **27**, 045015 (2018).
- ³⁴J. M. Kweun, H. J. Lee, J. H. Oh, H. M. Seung, and Y. Y. Kim “Transmodal Fabry-Pérot resonance: Theory and realization with elastic metamaterials,” *Phys. Rev. Lett.* **118**, 205901 (2017).
- ³⁵H. J. Lee, H. S. Lee, P. S. Ma, and Y. Y. Kim, “Effective material parameter retrieval of anisotropic elastic metamaterials with inherent non-locality,” *J. Appl. Phys.* **120**, 104902 (2016).
- ³⁶Z. J. Wong, Y. Wang, K. O’Brien, J. Rho, X. Yin, S. Zhang, N. Fang, T.-J. Yen, and X. Zhang, “Optical and acoustic metamaterials: Superlens, negative refractive index and invisibility cloak,” *J. Opt.* **19**, 084007 (2017).
- ³⁷Y. Y. Chen, G. K. Hu, and G. L. Huang, “A hybrid elastic metamaterial with negative mass density and tunable bending stiffness,” *J. Mech. Phys. Solids* **105**, 179–198 (2017).
- ³⁸R. Zhu, Y. Y. Chen, Y. S. Wang, G. K. Hu, and G. L. Huang, “A single-phase elastic hyperbolic metamaterial with anisotropic mass density,” *J. Acoust. Soc. Am.* **139**, 3303–3310 (2016).
- ³⁹R. Zhu, X. N. Liu, G. K. Hu, C. T. Sun, and G. L. Huang “Negative refraction of elastic waves at the deep-subwavelength scale in a single-phase metamaterial,” *Nat. Commun.* **5**, 5510 (2014).
- ⁴⁰Y. Li and B. M. Assouar, “Acoustic metasurface-based perfect absorber with deep subwavelength thickness,” *Appl. Phys. Lett.* **108**(6), 063502 (2016).
- ⁴¹Y. Y. Chen, G. L. Huang, and C. T. Sun, “Band gap control in an active elastic metamaterial with negative capacitance piezoelectric shunting,” *J. Vib. Acoust.* **136**(6), 061008 (2014).
- ⁴²Z. Hou and B. Assouar, “Tunable elastic parity-time symmetric structure based on the shunted piezoelectric materials,” *J. Appl. Phys.* **123**, 085101 (2018).
- ⁴³O. Thorp, M. Ruzzene, and A. Baz, “Attenuation and localization of wave propagation in rods with periodic shunted piezoelectric patches,” *Smart Mater. Struct.* **10**, 979–989 (2001).
- ⁴⁴Y. Y. Chen, R. Zhu, M. V. Barnhart, and G. L. Huang, “Enhanced flexural wave sensing by adaptive gradient-index metamaterials,” *Sci. Rep.* **6**, 35048 (2016).
- ⁴⁵G. Wang and S. Chen, “Large low-frequency vibration attenuation induced by arrays of piezoelectric patches shunted with amplifier–resonator feedback circuits,” *Smart Mater. Struct.* **25**, 015004 (2016).
- ⁴⁶L. Airoldi and M Ruzzene, “Design of tunable acoustic metamaterials through periodic arrays of resonant shunting piezos,” *New J. Phys.* **13**, 113010 (2011).
- ⁴⁷R. L. Forward, “Electronic damping of vibrations in optical structures,” *Appl. Opt.* **18**, 690–697 (1979).
- ⁴⁸S. Chen, G. Wang, J. Hong, and W. Sen, “Wave propagation and attenuation in plates with periodic arrays of shunted piezo-patches,” *J. Vib. Acoust.* **332**, 1520–1532 (2013).
- ⁴⁹F. Casadei, T. Delpero, A. Bergamini, P. Ermanni, and M. Ruzzene, “Piezoelectric resonator arrays for tunable acoustic waveguides and metamaterials,” *J. Appl. Phys.* **112**, 064902 (2012).
- ⁵⁰A. Bergamini, M. Zundel, E. A. Flores Parra, T. Delpero, M. Ruzzene, and P. Ermanni, “Hybrid dispersive media with controllable wave propagation: A new take on smart materials,” *J. Appl. Phys.* **118**, 154310 (2015).
- ⁵¹R. Zhu, Y. Y. Chen, M. V. Barnhart, G. K. Hu, C. T. Sun, and G. L. Huang, “Experimental study of an adaptive elastic metamaterial controlled by electric circuits,” *Appl. Phys. Lett.* **108**, 011905 (2016).